

Rationally designed universal passivator for high-performance single-junction and tandem perovskite solar cells

Received: 26 June 2024

Accepted: 8 January 2025

Published online: 17 January 2025

Check for updates

Zuolin Zhang^{1,8}, Yinsu Feng^{1,8}, Jike Ding^{1,8}, Quanxing Ma^{1,2,8}, Hong Zhang^{1,2} , Jiajia Zhang³ , Mengjia Li¹, Taoran Geng¹, Wenhuan Gao¹, Yang Wang⁴ , Boxue Zhang⁵, Thierry Pauporté⁵, Jian-Xin Tang⁶ , Hongjian Chen¹, Jiangzhao Chen⁷ & Cong Chen^{1,6}

Interfacial trap-assisted nonradiative recombination hampers the development of metal halide perovskite solar cells (PSCs). Herein, we report a rationally designed universal passivator to realize highly efficient and stable single junction and tandem PSCs. Multiple defects are simultaneously passivated by the synergistic effect of anion and cation. Moreover, the defect healing effect is precisely modulated by carefully controlling the number of hydrogen atoms on cations and steric hindrance. Due to minimized interfacial energy loss, L-valine benzyl ester p-toluenesulfonate (VBETS) modified inverted PSCs deliver a power conversion efficiency (PCE) of 26.28% using vacuum flash processing technology. Moreover, by suppressing carrier recombination, the large-area modules with an aperture area of 32.144 cm² and perovskite/Si tandem solar cells coupled with VBETS passivation deliver a PCE of 21.00% and 30.98%, respectively. This work highlights the critical role of the number of hydrogen atoms and steric hindrance in designing molecular modulators to advance the PCE and stability of PSCs.

Presently, several groups have achieved power conversion efficiency (PCE) exceeding 26% on emerging metal halide perovskite solar cells (PSCs), which makes it one of the most promising photovoltaic technologies^{1–3}. It is encouraging that perovskite/Si tandem solar cells (TSCs) demonstrated a tremendous PCE of 34.6%⁴. In recent years, inverted PSCs witnessed remarkable advancements in PCE and stability^{5–12}. However, the commercial deployment of single junction and tandem PSCs is hindered by their poor long-term operational

stability. Soft ionic lattice properties of perovskites make them suffer from poor intrinsic and extrinsic stabilities^{13,14}. The extrinsic stabilities can be overcome by developing advanced encapsulation technology¹⁵. However, the intrinsic instability induced by ion migration and deep-level defects is challenging to address^{8,16}. The defects within perovskite films can provide pathways for ion migration¹⁷. It was reported that the defect density at the interface of perovskite films is 1–2 orders of magnitude larger than that in the bulk of the films^{18,19}. Trap-assisted

¹State Key Laboratory of Reliability and Intelligence of Electrical Equipment, School of Materials Science and Engineering, Hebei University of Technology, Tianjin, China. ²State Key Laboratory of Photovoltaic Science and Technology, Shanghai Frontiers Science Research Base of Intelligent Optoelectronics and Perception, Institute of Optoelectronics, Fudan University, Shanghai, China. ³Anhui Provincial Key Laboratory of Green Carbon Chemistry, College of Chemistry and Materials Engineering, Fuyang Normal University, Fuyang, China. ⁴CAS Key Laboratory of Green Printing, Beijing National Laboratory for Molecular Science (BNLMS), Institute of Chemistry, Chinese Academy of Sciences, Beijing, China. ⁵Chimie ParisTech, PSL Research University, CNRS, Institut de Recherche de Chimie Paris (IRCP), UMR8247, 11 rue P. et M. Curie, Paris, France. ⁶Macao Institute of Materials Science and Engineering (MIMSE), Faculty of Innovation Engineering, Macau University of Science and Technology, Taipa, Macao, China. ⁷Faculty of Materials Science and Engineering, Kunming University of Science and Technology, Kunming, China. ⁸These authors contributed equally: Zuolin Zhang, Yinsu Feng, Jike Ding, Quanxing Ma.

e-mail: hzhangioe@fudan.edu.cn; jzhang@mail.ustc.edu.cn; wangyang@iccas.ac.cn; jxtang@must.edu.mo; jzchen@kust.edu.cn; chencong@hebut.edu.cn

nonradiative recombination, also called Shockley-Read-Hall (SRH), would reduce not only PCE but also long-term durability^{20,21}. Moreover, ion migration is much faster at grain boundaries (GBs) and interface than in the bulk of perovskite films^{19,22}. Therefore, it is of significant importance to enhance the PCE and intrinsic stability of PSCs by passivating interfacial defects and inhibiting interfacial ion migration via rational interface engineering.

The interface between the perovskite and electron transport layer (ETL) plays a critical role in realizing high-performance inverted PSCs. The C₆₀ and its derivatives (e.g., PC₆₁BM) are commonly used as ETL in inverted PSCs^{8,23}. Unfortunately, it was reported that the perovskite/ETL interface in inverted PSCs usually suffers from severe nonradiative recombination losses resulting from minority carriers and trap states^{24,25}. At this interface, there are usually various defects simultaneously encompassing positively charged defects (e.g., undercoordinated Pb²⁺ and halide vacancies) and negatively charged defects (such as cation vacancies and PbI₃⁻).²⁶ To effectively heal these harmful defects, a variety of interface materials have been developed, mainly involving low-dimensional perovskites^{27–29}, Lewis bases^{30–32}, organic cations³³, and organic salts^{8,24,34–36}. Compared with other interface materials, organic salts exhibit great potential in minimizing nonradiative recombination and suppressing ion migration due to their ability to simultaneously passivate positively and negatively charged defects^{8,24,35,36}. For example, Sargent et al.²⁴ synergistically used two types of organic ammonium salts propane-1,3-diammonium iodide (PDAl₂) and 3-(methylthio)propylaminehydroiodide (3MTPAI) to passivate the defects at upper interface in inverted PSCs, which achieved a certified quasi-steady-state PCE of 25.1%. To maximize the potential of organic salt modifiers, the rational design of organic anions and cations is of extreme importance. In terms of anions, halide anions (i.e., F⁻, Cl⁻, Br⁻, and I⁻) are frequently employed^{24,35,36}. However, nonhalide anions possess the advantages of adjustable structure and wide varieties as compared to halide anions.^{8,37} The organic anions containing -SO₃⁻³⁸ and -COO⁻⁸ have been certified to be capable of effectively passivating undercoordinated Pb²⁺ and halide vacancy defects and thus suppressing ion migration. Yang et al. demonstrated that p-toluenesulfonate stabilizes the perovskite interface by neutralizing negative work function shifts, reducing halide migration, and preventing charge accumulation, thereby enhancing the performance and stability of PSCs³⁹. Generally, cations can only passivate negatively charged defects through ionic bonds or electrostatic interaction. Our groups have revealed that multiple active site molecules are more effective in passivating trap states than single active site molecules^{3,40–42}. In order to increase the functions of cations and strengthen their interaction with perovskites, additional effective functional groups should be incorporated to functionalize cations. For instance, the introduction of Lewis base groups (e.g., -C=O and -SH) in organic cations should be able to passivate both negatively charged cation vacancy defects by ionic bond or hydrogen bond and positively charged undercoordinated Pb²⁺ and halide vacancy defects by coordination bond. Finally, the influencing mechanisms of the steric hindrance and the number of hydrogen atoms on cations on defect passivation remain blurry.

In this work, we proposed an effective defect passivation strategy by rational design of hydrogen atoms and steric hindrance of amino acid benzyl ester organic cations in nonhalide ammonium salts. The three amino acid salts, benzyl glycinate p-toluenesulfonate (BGTS), L-valine benzyl ester p-toluenesulfonate (VBETS), and L-leucine benzyl ester p-toluenesulfonate (LBETS), which have the same p-toluenesulfonate (TS⁻) nonhalide anion and different amino acid benzyl ester cations, were employed to passivate the upper surface of perovskite films in inverted PSCs. We found that the defect passivation effect of TS⁻ anions greatly depended on the steric hindrance induced by cation size. The only difference between the three cations (i.e., BG⁺, VBE⁺, and LBE⁺) is whether there is isopropyl or isobutyl substituent on BG⁺. We revealed that the

number of hydrogen atoms on cations exhibited a profound influence on defect passivation. The defect passivation effect of cations was determined by the balance between the number of hydrogen atoms and cation sizes. The multiple different active sites (TS⁻, -NH₃⁺, and -C=O) enabled simultaneous passivation of multiple defects, mainly including undercoordinated Pb²⁺, halide vacancy, and cation vacancy defects, which minimized interfacial nonradiative recombination losses. Through comprehensive consideration, VBETS was the most successful in passivating interfacial defects due to its appropriate number of hydrogen atoms and cation size. We also demonstrated that the VBETS can be used to passivate the defects of conventional and wide band gap (WBG) perovskite films, which confirmed the universality of this passivation strategy. The passivation of VBETS is generally suitable for improving the efficiency of single-junction and tandem PSCs.

Results

Theoretical screening of organic cations

Figure 1a shows the chemical structures and electrostatic potential (ESP) of three sorts of cations and TS⁻ anions. All organic salts have TS⁻, -NH₃⁺, and -C=O active sites, which should be able to simultaneously manage various positively and negatively charged defects. Density functional theory simulation was performed to investigate the defect passivation effect of three organic nonhalide ammonium salts for the surface of perovskite films. As illustrated in Fig. 1b and Supplementary Figs. 1–3, we explored the passivation effect of different organic salts for various defects, including Pb²⁺, substituted I (Pb_i), I vacancy (V_I), and FA⁺ vacancy (V_{FA}). It was found that the three salts can passivate these defects, but VBETS and LBETS were better than BGTS regardless of defect types, which could be because of the introduction of alkyl substituent. For positively charged Pb_i (Supplementary Fig. 1a–c) and V_I (Supplementary Fig. 2a–c), the defect passivation effect increased in the order of BGTS, VBETS, and LBETS, which is consistent with the cation size order of BG⁺ < VBE⁺ < LBE⁺. In our previous work, we have uncovered that the size of imidazolium cations can markedly impact the defect passivation effect of BF₄⁻ anions⁴³. The large-sized cation would weaken the Coulomb force between the cation and anion due to large steric hindrance, heightening the interaction of anions with perovskites^{43–45}.

Regarding negatively charged V_{FA} defects (Supplementary Fig. 3a–c), the defect passivation order of BG⁺ < LBE⁺ < VBE⁺ was observed. This means incorporating an alkyl substituent can promote the defect passivation of cations for V_{FA} defects. From the perspective of steric hindrance, the smaller cation size is more beneficial for passivating V_{FA} defects. However, this is the opposite of our experimental results. Therefore, we speculated that the other factor exerts a highly positive role in passivating V_{FA} defects, which counteracts the negative effect of steric hindrance. Subsequently, we focused on delving into the passivation effect of three different cations for the V_{FA} defects. Figure 1c–e presents that the binding energies of BG⁺, VBE⁺, and LBE⁺ cations with FAPbI₃ perovskites containing V_{FA} defects are -4.62 eV, -5.15 eV, and -4.91 eV, respectively. This indicates that the cations' passivation order agrees with the salt molecule passivation order. Obviously, the VBE⁺ showcased the optimal passivation effect for V_{FA}. To study the reason behind the phenomenon, we systematically compared the binding energies of NH₄⁺ (An⁺), CH₃NH₃⁺ (MA⁺), CH₃CH₂NH₃⁺ (EA⁺), BG⁺, VBE⁺ and LBE⁺ with FAPbI₃ perovskites containing V_{FA} defects (Fig. 1f and Supplementary Fig. 4a–f). It was found that the binding energy gradually increased as the number of hydrogen atoms on alkyl increased. We inferred that hydrogen atoms on alkyl had strong electrostatic interaction with V_{FA} defects and/or [PbI₆]²⁻ octahedron, which was further verified by the charge density difference of BG⁺, VBE⁺, and LBE⁺ with FAPbI₃ surface encompassing V_{FA} defects (Fig. 1g–i and Supplementary Fig. 5a–c). It can be concluded that the defect passivation effect of cations was determined by the compromise between the number of hydrogen atoms and steric

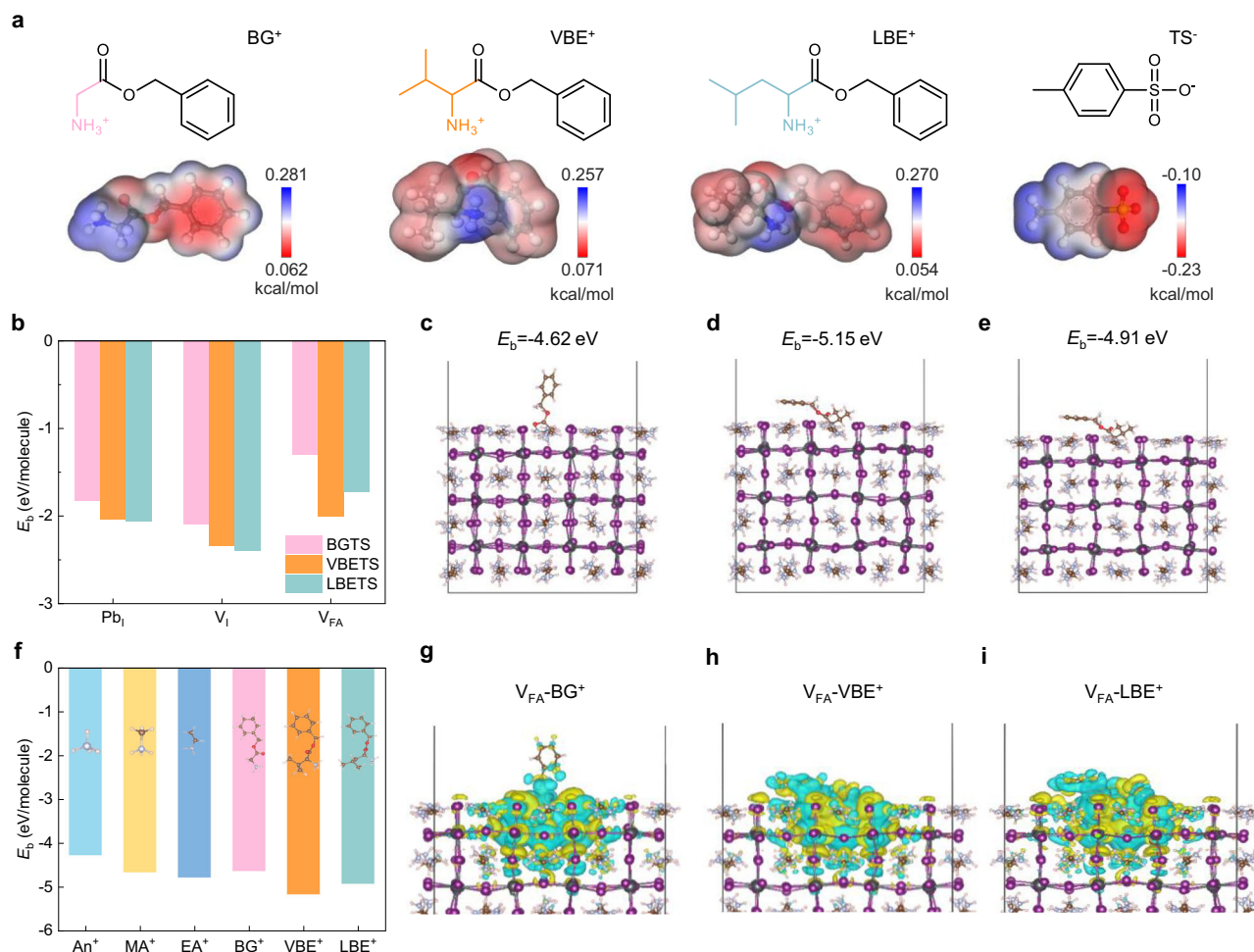


Fig. 1 | Theoretical screening of organic cations. **a** The chemical structures and electrostatic potential of BG⁺, VBE⁺, LBE⁺, and TS⁻. **b** The binding energy of BGTS, VBETS, and LBETS with FAPbI₃ containing Pb_I anti-site, V_I, and V_{FA} defects. **c–e** The binding energy of (c) BG⁺, (d) VBE⁺, and (e) LBE⁺ cations with FAPbI₃ containing V_{FA}

defects. **f** Binding energy of An⁺, MA⁺, EA⁺, BG⁺, VBE⁺, and LBE⁺ with FAPbI₃ containing V_{FA} defects. **g–i** Charge density difference of (g) BG⁺, (h) VBE⁺, and (i) LBE⁺ with FAPbI₃ surface encompassing V_{FA} defects (cyan indicates a decrease in charge density, yellow indicates an increase in charge density).

hindrance. The proper number of hydrogen atoms and steric hindrance are necessary for achieving optimal defect passivation.

Experimental screening of organic cations via investigating interactions

It needs to be pointed out that the 1.58 eV-Cs_{0.05}(FA_{0.95}MA_{0.05})_{0.95}Pb(I_{0.95}Br_{0.05})₃ perovskite was used to investigate the interaction of modifiers with perovskite and the effect of interface modification on the optoelectronic properties of perovskite films. We further experimentally analyzed the chemical interactions of three organic ammonium salts with the perovskite. As shown from the X-ray photoelectron spectroscopy (XPS) in Fig. 2a, the BGTS, VBETS, and LBETS modified perovskite films exhibited S 2p characteristic peaks, indicating that all modification molecules have been successfully introduced into the upper surface of the perovskite films. At the same time, VBETS exhibited the maximum peak shift, demonstrating the maximum variation in the chemical environment and binding energy of -C=O in cations and -S=O in anions with undercoordinated Pb²⁺ and/or V_I defects. It revealed that BGTS, VBETS, and LBETS exhibited peak shifts of 0.4 eV, 0.6 eV, and 0.5 eV, respectively. The largest peak shift of 0.6 eV indicates that VBETS had the best passivation effect for Pb-

related defects through the synergistic coordination of -C=O and -S=O in anions and cations due to appropriate cation size and steric hindrance. The shift of the I 3d binding energy peak indicates that hydrogen bonds were formed between -NH₃⁺ in the three organic ammonium salt molecules and I⁻ in [PbI₆]⁴⁻ in perovskite, which is conducive to filling the V_{FA} vacancy defects in octahedral crystals and stabilizing perovskite crystals.⁴⁶ Additionally, the electrostatic interaction of the hydrogen atoms on the alkyl group with I⁻ on [PbI₆]⁴⁻ octahedron should also be responsible for the shifted binding energy of I 3d peaks, which has been confirmed by theoretical calculation results. As shown in the Fourier transform infrared spectroscopy (FTIR) in Fig. 2d–f, the C=O peak was shifted from 1749 cm⁻¹ of BGTS to 1751 cm⁻¹ of BGTS+PbI₂, from 1748 cm⁻¹ of VBETS to 1735 cm⁻¹ of VBETS+PbI₂, and from 1746 cm⁻¹ of LBETS to 1741 cm⁻¹ of LBETS+PbI₂, suggesting the coordination bonds between C=O and Pb²⁺. In a similar way, the shift of S=O from 1033 cm⁻¹ of BGTS to 1038 cm⁻¹ of BGTS+PbI₂, from 1038 cm⁻¹ of VBETS to 1022 cm⁻¹ of VBETS+PbI₂, and from 1035 cm⁻¹ of LBETS to 1025 cm⁻¹ of LBETS+PbI₂ affirmed the coordination interaction of S=O with Pb²⁺. In short, combining XPS and FTIR confirmed the interaction of C=O and S=O with Pb²⁺.

Characterization of perovskite films

The above experimental and theoretical results certified the chemical interaction between organic salt modifiers and perovskites as well as their passivation ability for various defects. Then, we conducted a

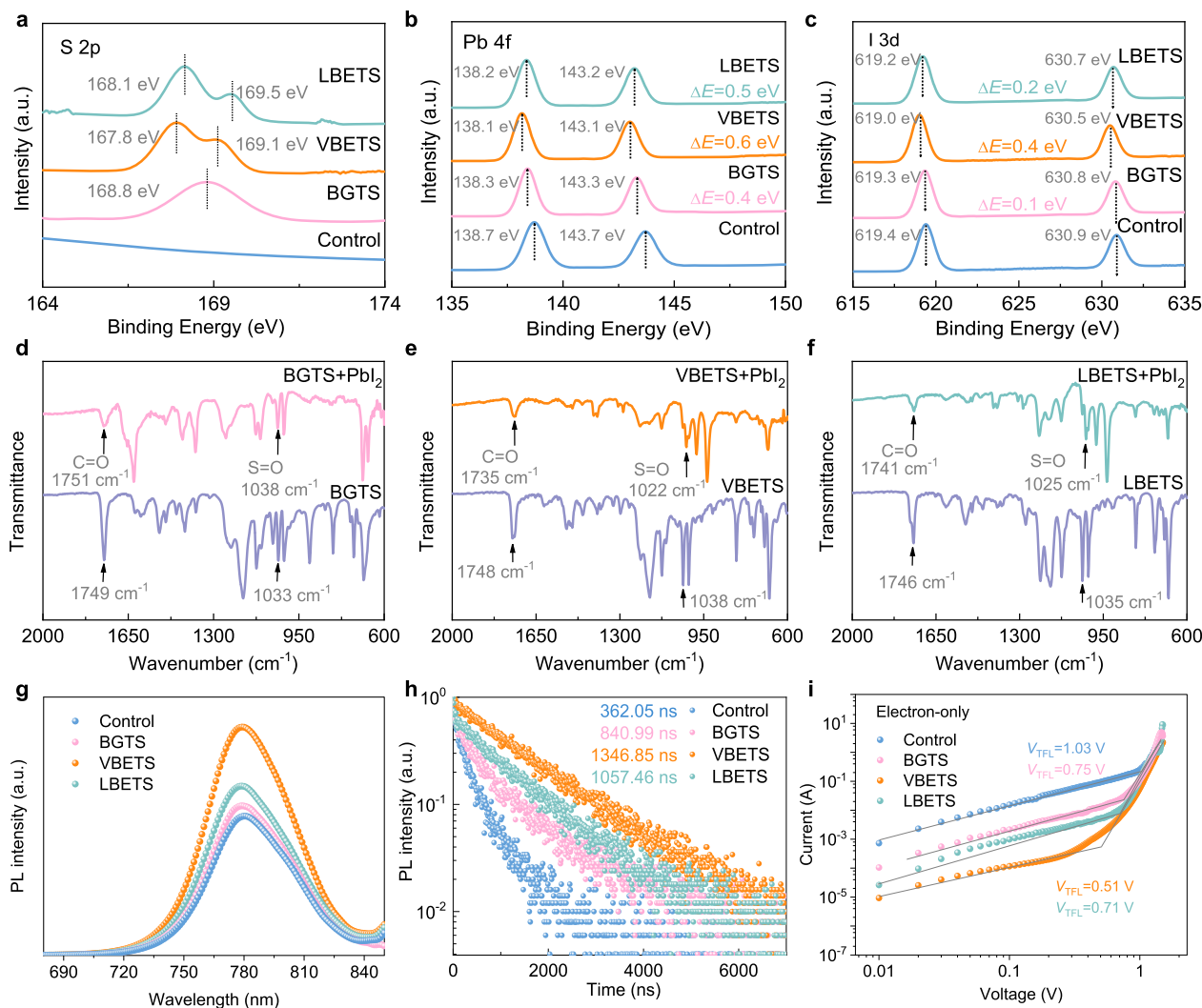


Fig. 2 | Chemical interactions and perovskite film quality. **a** XPS spectra of S 2p in the control and BGTS, VBETS, or LBETS-modified perovskite films. **b, c** XPS spectra of **(b)** Pb 4f and **(c)** I 3d in control and BGTS, VBETS, or LBETS modified perovskite films. **d-f** FTIR for **(d)** BGTS and BGTS+PbI₂, **(e)** VBETS and VBETS+PbI₂, and **(f)**

LBETS and LBETS+PbI₂. **g, h** Steady-state PL **(g)** and TRPL **(h)** spectra of the control, BGTS, VBETS, and LBETS-modified perovskite films on a bare glass substrate. **i** *I*-*V* curves of the devices based on ITO/SnO₂/perovskite (BGTS, VBETS, and LBETS)/C₆₀/Ag structure under dark.

qualitative and quantitative analysis of the defects through spectroscopic and electrical means. A 475 nm laser excitation was employed to measure the steady-state photoluminescence (PL) and time-resolved photoluminescence (TRPL) of perovskite films on bare glass. As shown in Fig. 2g, the PL intensities of the samples gradually increased according to this order of the control, BGTS, LBETS, and VBETS-modified perovskite films, indicating the lowest trap density in the VBETS-modified sample. The TRPL results in Fig. 2h show that the average lifetimes of the control, BGTS-, VBETS-, and LBETS-passivated perovskite films were 362.05 ns, 840.99 ns, 1346.85 ns, and 1057.46 ns, respectively. Among all samples, the VBETS-modified perovskite film had the longest average carrier lifetime and strongest PL intensity, indicating its excellent defect healing function, which minimized nonradiative recombination losses. Much reduced nonradiative recombination should be conducive to enhancing open-circuit voltage (*V*_{OC}) and fill factor (FF) as well as reinforcing device stability.

To further evaluate the passivation effects of different modification molecules from a quantitative perspective, we calculated the trap state density of perovskite films by the space charge limited current (SCLC) method. According to the formula of $N_t = 2\epsilon_0\epsilon_r V_{TFL}/qL^2$ ⁴⁷, the value of *V*_{TFL} is positively correlated with the value of trap state density. SCLC results based on electron transporting-only devices (ITO/SnO₂/

perovskite/C₆₀/Ag) revealed that the *V*_{TFL} of control, BGTS, VBETS, and LBETS-modified devices are 1.03 V, 0.75 V, 0.51 V and 0.71 V (Fig. 2i), while the results based on hole transporting-only devices (ITO/NiO_x/perovskite/Spiro-OMeTAD/Ag) revealed that the *V*_{TFL} was 0.67 V, 0.66 V, 0.53 V, 0.58 V (Supplementary Fig. 6). After BGTS, VBETS, and LBETS passivation, the electron defect density was reduced from 13.2 × 10¹⁵ cm⁻³ to 9.6 × 10¹⁵ cm⁻³, 6.5 × 10¹⁵ cm⁻³, and 9.1 × 10¹⁵ cm⁻³, and hole defect density was decreased from 8.6 × 10¹⁵ cm⁻³ to 8.5 × 10¹⁵ cm⁻³, 6.8 × 10¹⁵ cm⁻³, and 7.4 × 10¹⁵ cm⁻³, indicating that VBETS can efficiently passivate the multiple defects on the surface of perovskite films.

From the perspective of macroscopic thin film and crystal morphology, the effects of BGTS, VBETS, or LBETS modification on the morphology of 1.58 eV-Cs_{0.05}(FA_{0.95}MA_{0.05})_{0.95}Pb(I_{0.95}Br_{0.05})₃ perovskite films were analyzed by scanning electron microscopy (SEM) in Fig. 3a. There are many white PbI₂ phase and pores on the surface of the pristine perovskite film, while the white PbI₂ phase and pores were reduced after BGTS, VBETS, and LBETS modification⁴⁸. The same results were obtained in the SEM images of wide bandgap 1.66 eV-Cs_{0.05}MA_{0.15}FA_{0.8}Pb(I_{0.76}Br_{0.24})₃ perovskites (crystallization on a monocrystalline Si substrate) for the reduction of excess PbI₂ phase impurities after the modification of BGTS, VBETS, or LBETS (Supplementary Fig. 7a–d). Among them, the VBETS-modified perovskite film

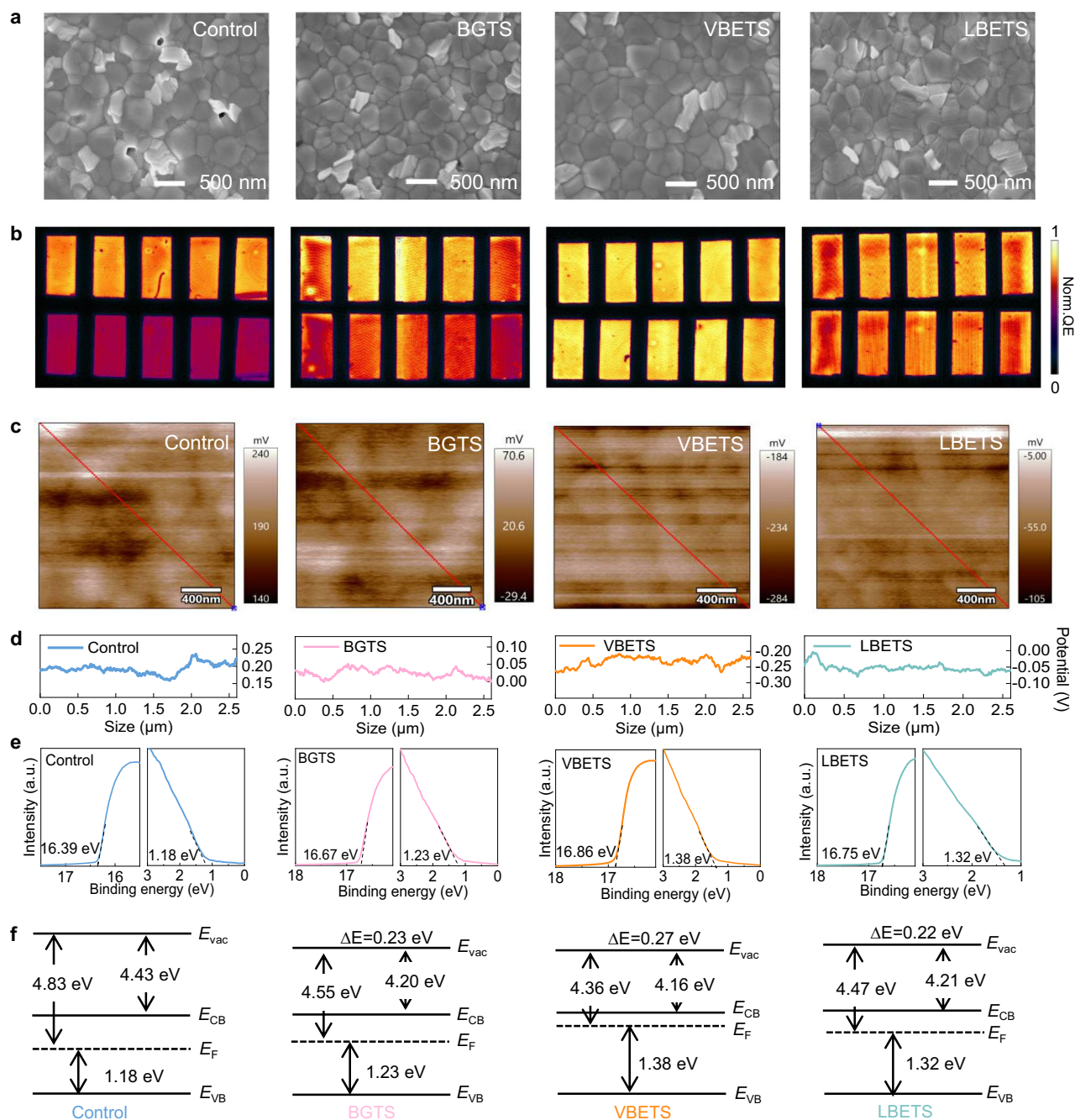


Fig. 3 | Surface potentials and energy level of perovskite films. a SEM images of the control, BGTS, VBETS, and LBETS-modified 1.58 eV- $\text{Cs}_{0.05}(\text{FA}_{0.95}\text{MA}_{0.05})_{0.95}\text{Pb}(\text{I}_{0.95}\text{Br}_{0.05})_3$ perovskite films. **b** LBIC mapping images of the control, BGTS-, VBETS-, and LBETS-modified 1.58 eV- $\text{Cs}_{0.05}(\text{FA}_{0.95}\text{MA}_{0.05})_{0.95}\text{Pb}(\text{I}_{0.95}\text{Br}_{0.05})_3$ based PSCs, the top row is fresh perovskite films and the bottom row is perovskite films after aging for 5 days at room temperature under RH of $60 \pm 10\%$. **c** KPFM images of

the control, BGTS, VBETS, and LBETS-modified 1.58 eV- $\text{Cs}_{0.05}(\text{FA}_{0.95}\text{MA}_{0.05})_{0.95}\text{Pb}(\text{I}_{0.95}\text{Br}_{0.05})_3$ perovskite films. **d** Tangent lines in KPFM images to demonstrate changes in surface potential. **e** UPS spectra of the control, BGTS, VBETS, and LBETS-modified perovskite films. **f** Energy level diagram of the control and BGTS, VBETS, and LBETS-modified perovskite films.

exhibited the flattest surface morphology with lowest root mean square roughness of 15.22 nm, lower than that of 19.68 nm, 17.34 nm and 16.04 nm for control, BGTS, and LBETS modified perovskite films, as exhibited in the atomic force microscope (AFM) images in Supplementary Fig. 8a–d. This could be ascribed to the strongest interaction of VBETS with perovskites. The flat and uniform perovskite film will promote electron extraction at the perovskite/ETL interface and reduce nonradiative recombination losses⁴⁹.

The defect distribution and density were further characterized by laser beam-induced current (LBIC) imaging technology, which used a

laser beam to scan the surface of the PSCs to reveal the photocurrent mapping and generate the internal trap defect distribution of the device on a macroscopic scale⁵⁰. As shown in Fig. 3b, the LBIC results show that the control film exhibited very poor film uniformity and low photon current response, while all modified devices presented enhanced film uniformity and current. VBETS-modified devices exhibited the highest current due to their best defect passivation effect. Further, the surface current of the control devices decreased significantly after aging at room temperature under relative humidity (RH) of $60 \pm 10\%$ for 5 days, while the surface current of the VBETS-

modified PSCs decayed slightly. Moreover, the slowest decay was found in the VBETS-modified devices.

Kelvin probe force microscopy (KPFM) measurement was carried out to gain insights into the surface potentials of the perovskite films. As shown in Fig. 3c, d, the average surface potential of the control, BGTS, VBETS, and LBETS-modified perovskite films was 196.64 mV, 22.92 mV, -233.22 mV and -53.46 mV, respectively. It was revealed that the VBETS-modified perovskite film exhibited the lowest surface potential with the largest difference up to 430 mV compared with the control perovskite film. As shown from the ultraviolet photoelectron spectroscopy (UPS) (Fig. 3e) and corresponding bandgap structure schematic diagram (Fig. 3f), we can conclude that the Fermi energy levels of the BGTS, VBETS, and LBETS modified perovskite films shifted upward compared with the control perovskite film. Particularly, VBETS-modified perovskite films exhibited a most obviously shifted Fermi energy, indicating that VBETS modification induced more n-type characteristics³³. This is related to the reason that VBETS passivated the electronic defects on the surface of the perovskite and formed a back surface field with the bulk phase of the perovskite. The formed back surface field is in the same direction as the built-in electric field of the device, thus making the stronger built-in potential (V_{bi}) of 0.95 V, which is higher than 0.87 V for control devices from the Mott-Schottky plots (Supplementary Fig. 9a, b), thus promoting electron transport and extraction⁵¹. Actually, organic cation-induced n-type doping and back electric field at perovskite/ETL interface have been reported to improve the PCE and stability of inverted PSCs³³.

Investigation of photovoltaic performance

To assess the photovoltaic performance of PSCs, we fabricated p-i-n type NiO_x -based inverted PSCs device, where BGTS, VBETS, and LBETS were used to modify the upper surface of perovskite films. Specifically, to verify the universality of our surface passivation strategy, we adopted conventional bandgap perovskites of 1.53 eV and 1.58 eV perovskite, as well as a WBG 1.66 eV perovskite as light-harvesting materials. The comparative analysis of the optimized concentrations of three passivating agents of BGTS, VBETS, and LBETS for modifying the perovskites is located at 0.5 mg/mL in an isopropanol solution (Supplementary Fig. 10a–c). The cross-sectional SEM image of the VBETS-modified 1.53 eV-perovskite based PSC device is shown in Supplementary Fig. 11, revealing the good crystallinity and clear functional layer interface. Supplementary Fig. 12a–d shows statistical data of all photovoltaic parameters (PCE, V_{OC} , J_{SC} , and FF) from 1.53 eV PSCs. VBETS-modified PSCs exhibited higher average PCE values of 24.93%, respectively, higher than 23.01% for the control devices. Figure 4a and Supplementary Fig. 13 present the typical J - V curves of the best-performing control BGTS, VBETS, and LBETS-modified 1.53 eV PSC devices in reverse scan (RS) and forward scan (FS) testing modes. It was revealed that the control, BGTS, VBETS, and LBETS-modified PSCs delivered a champion PCE of 23.44%, 23.82%, 25.26% and 24.77%, respectively. We also achieved an attractive certified PCE of 25.15% (J_{SC} of 25.68 mA cm^{-2} , a V_{OC} of 1.191 V, and an FF of 82.28%) in RS and a certified value of 24.95% (J_{SC} of 25.75 mA cm^{-2} , a V_{OC} of 1.184 V, and an FF of 81.84%) in FS (Supplementary Figs. 14–20). To the best of our knowledge, our obtained certified PCE value of 25.15% is the record result reported for the inverted PSCs based on the vacuum flash method in ambient conditions for perovskite deposition (Supplementary Table 1). In addition, the hysteresis index (HI = $(\text{PCE}_{\text{Reverse}} - \text{PCE}_{\text{Forward}}) / \text{PCE}_{\text{Reverse}}$) was 4.39%, 2.73%, 1.15%, and 2.26% for the control, BGTS, VBETS, and LBETS-modified PSCs, respectively (Supplementary Table 2). The smallest hysteresis for the VBETS-modified PSCs could have resulted from reduced defect density and facilitated interfacial electron extraction, thus suppressing interfacial charge accumulation. We also prepared PSC devices based on 1.53 eV perovskite in an N_2 atmosphere using VBETS as a passivator. The J - V curve results

(Fig. 4b) show that the VBETS-modified device can achieve champion efficiency values of 26.28% (J_{SC} of 26.13 mA cm^{-2} , a V_{OC} of 1.191 V, and an FF of 84.45%) in RS mode and 26.23% (J_{SC} of 26.13 mA cm^{-2} , a V_{OC} of 1.191 V, and an FF of 84.28%) in FS mode, which are much higher than the efficiency values of 24.64% (J_{SC} of 25.71 mA cm^{-2} , a V_{OC} of 1.178 V, and an FF of 81.36%) and 24.57% (J_{SC} of 25.71 mA cm^{-2} , a V_{OC} of 1.178 V, and an FF of 81.13%) of the control device.

Our developed passivation approach is also effective for the 1.58 eV and WBG 1.66 eV-based PSCs prepared by using vacuum flash technology in ambient conditions. As is seen in Supplementary Fig. 21, the champion J - V curves indicate that VBETS passivation leads to an increased PCE from 21.69% to 23.52% for the 1.58 eV PSCs. Further, VBETS modification helped to achieve an enhanced PCE from 20.79% to 21.75% in the WBG 1.66 eV-based PSCs (Fig. 4c), accompanied by increased V_{OC} and FF together with slightly improved J_{SC} . This indicates that our surface passivation method suits both conventional bandgap and WBG 1.66 eV-PSCs. The statistical chart of J_{SC} , FF, V_{OC} , and PCE (Fig. 4d and Supplementary Figs. 12, 22–23) of the devices with different components reveals that VBETS modification could help to improve all the photovoltaic performance in PSCs, proving the universality and versatility of VBETS passivator. The integrated J_{SC} from the EQE of devices modified by VBETS all show a certain degree of increase, regardless of the type of perovskite system (Supplementary Figs. 24–26). Specifically, the integrated J_{SC} values of the champion PSCs with band gaps of 1.53 eV, 1.58 eV, and 1.66 eV are 25.74 mA cm^{-2} , 24.56 mA cm^{-2} , and 20.42 mA cm^{-2} , respectively (Fig. 4e). We then fabricated a large-area module by vacuum flash method to verify the effectiveness and universality of VBETS passivation, where 14 subcells were connected in series. The champion VBETS-modified PSC module with an aperture area (including dead area) of 32.144 cm^2 achieved a PCE of 21.00% (Fig. 4f). Calculating by the active area of 30.408 cm^2 (which accounts for 94.6% of the aperture area), we obtained an efficiency of 22.20%. According to the statistics, these results are all the highest efficiency reported for the large-area modules with an area over 30 cm^2 (Fig. 4g and Supplementary Table 3).

To investigate the charge carrier recombination lifetime (τ_r) and carrier transport lifetime (τ_t) of PSC devices, transient photovoltage (TPV) and transient photocurrent (TPC) measurements were performed on the control and VBETS-modified devices.⁵² Supplementary Fig. 27 shows that the VBETS-modified device exhibited a τ_r value of 2.59 μs , more than twice as long as that of the control device (1.24 μs). In addition, it can be seen that VBETS-modified devices exhibited a τ_t value of 0.50 μs (Supplementary Fig. 28), which is dramatically shorter than that of 1.66 μs for the control devices. As shown in Supplementary Fig. 29, the -3dB bandwidth ($f_{-3\text{dB}}$) of VBETS-modified devices was 0.40 MHz, which is much larger than the 0.10 MHz of the control devices, indicating that VBETS-modified devices have faster charge carrier transport and light response³³. After VBETS modification, the reduced defect density and improved energy band alignment should account for promoted carrier transport and extraction. Electrochemical impedance spectroscopy (EIS) measurements (Supplementary Fig. 30) further revealed the ameliorated charge transport and inhibited nonradiative recombination following VBETS passivation. V_{OC} as a function of light intensity measurements (Supplementary Fig. 31) revealed that the ideal factor (1.24) of the VBETS-modified device is closer to 1 than that of the control device (1.43), indicating the reduced SRH recombination associated with the trap defects⁵⁴. We also performed PL and TRPL of the glass/perovskite (1.53 eV, 1.58 eV and 1.68 eV)/ C_{60} samples to gain deeper insights into the carrier extraction capabilities in PSC devices (Supplementary Fig. 32a–f). The modification of VBETS can reduce PL intensity and decay lifetime for all bandgap perovskite samples, which is indicative of facilitated electron extraction and transfer at perovskite/ C_{60} interface.

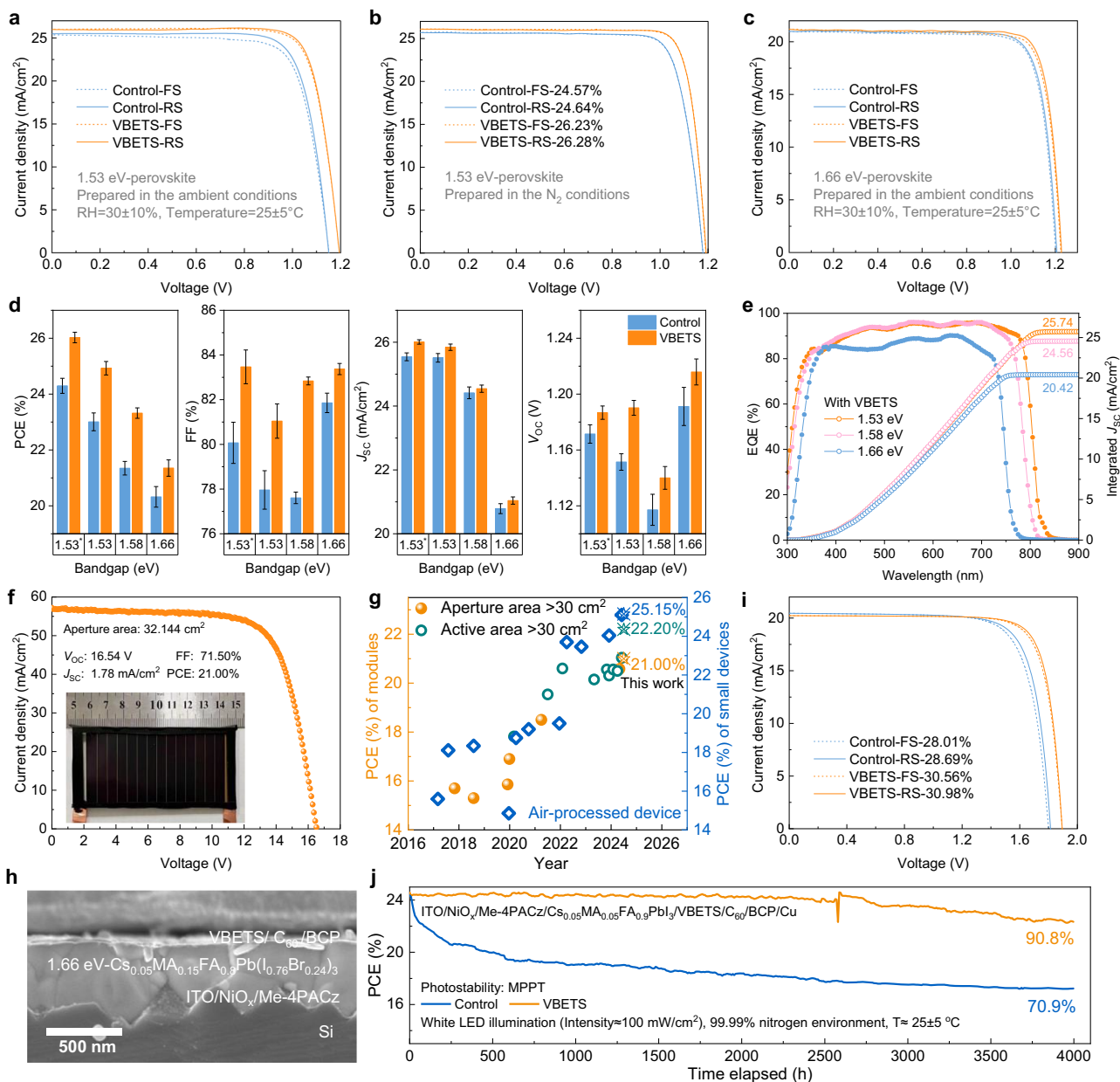


Fig. 4 | Device performance and long-term stability. **a–c** Champion J - V curves of the best-performing control and VBETS-modified **(a)** 1.53 eV (prepared in the ambient conditions), **(b)** 1.53 eV (prepared in the glovebox with 99.999% N₂ conditions), and **(c)** 1.66 eV perovskite-based PSC devices in reverse and forward scan mode. **d** The column-shaped statistical chart of PCE, V_{OC} , J_{SC} , and FF parameters for control devices and VBETS-modified devices based on 1.53 eV, 1.58 eV, and 1.66 eV perovskite as photoactive layer. Specifically, * represents that perovskite devices are prepared in N₂ glove boxes, while the others are prepared under air ambient conditions. **e** The EQE spectra and integrated J_{SC} of the champion VBETS-modified

PSCs with 1.53 eV, 1.58 eV, and 1.66 eV perovskites. **f** J - V curves of the 1.58 eV-perovskite-based PSC modules with VBETS modification. The inset is the photograph of a VBETS-modified perovskite module with an aperture area of 32.144 cm². **g** Comparison of the historical PCEs of the PSC module with an aperture area exceeding 30 cm². **h** Cross-sectional SEM image for exhibiting the device structure of perovskite/HJT crystalline silicon TSCs modified with VBETS. **i** J - V curves for the TSCs without and with VBETS in reverse and forward scan mode. **j** MPPT stability curves of the single-junction PSCs without and with VBETS.

Based on WBG 1.66 eV perovskite as the top-subcells with VBETS passivation, we fabricated perovskite/silicon TSCs, where the bottom cell is 1.1 eV crystalline silicon (Si) heterojunction (HJT) solar cells. The SEM cross-sectional view and overall structural schematic diagram of the TSCs are shown in Fig. 4h and Supplementary Fig. 33. Precisely, the magnetron sputtering method was applied on a heterojunction Si substrate to prepare transparent ITO as the top transparent conductive electrode. As is exhibited in Fig. 4i, the champion efficiency of the VBETS-passivated tandem device was achieved at 30.98% (with a V_{OC} of 1.89 V, a J_{SC} of 20.23 mA cm⁻², and an FF of 80.76%) in the RS, and 30.56% (with a V_{OC} of 1.895 V, a J_{SC} of 20.23 mA cm⁻² and an FF of

79.73%) in the FS. These efficiency values are much higher than that of 28.69% (with a V_{OC} of 1.816 V, a J_{SC} of 20.44 mA cm⁻², and an FF of 77.29%) in RS and 28.01% (with a V_{OC} of 1.797 V, a J_{SC} of 20.44 mA cm⁻², and an FF of 76.25%) in FS for the control tandem solar cells. The effective enhancement of TSC devices comes from the improved V_{OC} , demonstrating the effective role of VBETS interface defect passivation in suppressing nonradiative recombination. The EQE spectra in Supplementary Fig. 34 revealed that the integrated J_{SC} of the VBETS-modified WBG PSCs and filtered SHJ devices were 20.28 mA cm⁻² and 20.13 mA cm⁻², respectively, which are consistent with the J_{SC} values from J - V curves.

Study of long-term stability

We assessed the operational stability of single-junction PSCs and perovskite/Si TSCs without and with VBETS passivation. We conducted the maximum power point tracking (MPPT) of the control and VBETS-modified devices under continuous 100 mW cm⁻² white LED light irradiation at room temperature of 25 ± 5 °C and stored in a 99.99% nitrogen environment. As for the 1.53 eV-Cs_{0.05}MA_{0.05}FA_{0.9}PbI₃-based single-junction PSCs, encapsulation using glass front with UV-curable adhesive encapsulant for sealing was applied, as is shown in Fig. 4j, after 4000 h of continuous light exposure, the VBETS-modified device could retain 90.8% of the initial PCE, while the control device dropped to 70.9% under the same conditions. The improved light stability of VBETS-modified devices is mainly associated with reducing trap defects at surface and grain boundaries. The TSCs were then subjected to stability measurements at room temperature and under white light illumination with internal cyclic *J-V* tests with a scanning interval of 124.8 mins. As illustrated in Supplementary Fig. 35, the VBETS-modified TSCs could maintain 94.2% of the initial PCE value after 1030 h of aging. The overall output characteristics and stability of the device are higher than those of the control TSC device. It was revealed that VBETS modification can enhance the operational stability of single junction and TSCs due to reduced surface defect density by synergistic passivation of nonhalide anion and organic cations.

Meanwhile, the effect of VBETS modification on the long-term stability of PSCs was investigated systematically. The encapsulated PSCs are stored in ambient conditions (RH = 35 ± 5%, Temperature = 25 ± 5 °C). Supplementary Fig. 36a–d compares the results of the long-term stability of the 1.53 eV, 1.58 eV, 1.66 eV-based single-junction PSCs and perovskite/Si TSCs without and with VBETS passivation. It can be observed that, whether in single-junction or tandem devices, the VBETS-modified devices exhibit higher stability than the control devices. The 1.66 eV-PSCs and TSCs degrade at faster rates, correlating with the inherently poor stability of the WBG perovskite with a high bromide (Br) ratio. The contact angles of the control, BGTS, VBETS, and LBETS-modified perovskite films are 30.1°, 31.4°, 43.3°, and 45.1°, respectively. VBETS and LBETS, due to their longer cationic alkyl chains, exhibit stronger hydrophobic characteristics, which in turn contribute to improved moisture resistance of the films and enhanced device stability (Supplementary Fig. 37a–d).

In summary, we have developed a universal passivation strategy for organic ammonium salt molecules containing nonhalide organic anions, minimizing energy loss at the upper interface in inverted PSCs through the rational design of the number of hydrogen atoms on cations and steric hindrance. The synergistic effect of anions and cations enabled the simultaneous passivation of positively charged and negatively charged defects and the modulation of interface bands. VBETS possessing an appropriate number of hydrogen atoms and cation size exhibited the best effect in defect passivation and energy band modulation. The universality of this passivation strategy was confirmed by using different bandgap perovskites. Finally, the VBETS-modified inverted PSCs based on conventional 1.53 eV bandgap perovskite yielded a PCE of 25.26% prepared in ambient conditions and 26.28% prepared in an N₂-preparing atmosphere. The perovskite/Si TSCs coupled with VBETS passivation demonstrated a promising PCE of 30.98%. This work highlights the critical role of the number of hydrogen atoms and steric hindrance in designing multisite nonhalide ammonium salts to improve the PCE and stability, which lays the groundwork for the development of perovskite photovoltaics.

Methods

Materials

Formamidinium iodide (FAI), methylammonium iodide (MAI), methylamine hydrochloride (MACl), methylammonium bromide (MABr) were purchased from Greatcell Solar Materials. Lead chloride (PbCl₂ 99.5%) were purchased from Xi'an Bright Optoelectronics Technology Co.,

Ltd. Lead iodide (PbI₂, 99.999%), cesium iodide (CsI, 99.99%) and lead bromide (PbBr₂ 99.999%) were purchased from Chengdu Alpha Metal Materials Co., Ltd.. N,N-dimethylformamide (DMF, 99.9%), Dimethyl sulfoxide (DMSO) and 1-methyl-2-pyrrolidinone (NMP, 99.9%) were purchased from MACKLIN. [2-(9H-Carbazol-9-yl)ethyl]phosphonic Acid (2PACz, >98.0% HPLC) and [4-(3,6-Dimethyl-9H-carbazol-9-yl)butyl]phosphonic Acid (Me-4PACz, >99.0% HPLC) was purchased from TCI; BCP, PC₆₁BM, C₆₀ were purchased from Advanced Election Technology. The three amino acid salts, benzyl glycinate p-toluenesulfonate (BGTS), L-valine benzyl ester 4-toluenesulfonate (VBETS), and L-leucine benzyl ester p-toluenesulfonate salt (LBETS) was obtained from MACKLIN.

Nickel(II) nitrate hexahydrate (Ni(NO₃)₂·6H₂O) was purchased from Sigma-Aldrich for synthesizing the NiO_x nanoparticles. All chemicals were used without further purification. NiO_x nanoparticles were synthesized as follows: Firstly, 3 g of Ni(NO₃)₂·6H₂O was dissolved in 50 mL of deionized (DI) water. The solution was stirred at room temperature for 30 min. Subsequently, a 1.0 M NaOH solution was slowly added with continuous magnetic stirring until the pH reached approximately 10. After an additional hour of stirring, a green precipitate was obtained via centrifugation at 9000 rpm for 6 min. The precipitate was washed three times with DI water. The collected green solid was frozen for 3 h, then freeze-dried at 5 Pa for 15 h, and finally calcined at 270 °C for 2 h to produce NiO_x nanoparticles. Prior to use, the NiO_x was dispersed in DI water by sonication for 10 min at a concentration of 30 mg/mL.

Preparation of perovskite precursor solutions and film deposition

1.53 eV-Cs_{0.05}MA_{0.05}FA_{0.9}PbI₃: The stoichiometric Cs_{0.05}MA_{0.05}FA_{0.9}PbI₃ precursor solution was prepared by dissolving 20.784 mg of CsI, 247.68 mg of FAI, 12.72 mg of MAI, 15 mg of MACl, 11.124 mg of PbCl₂, and 785.55 mg of PbI₂ in 1 ml mixed solvent of DMF/DMSO (4:1, by volume). For the 1.53 eV-Cs_{0.05}MA_{0.05}FA_{0.9}PbI₃ film crystallization, the perovskite films were deposited by spin-coating the perovskite precursor solution on glass/ITO/NiO_x/Me-4PACz substrate at 1000 rpm for 10 s and 5000 rpm for 30 s. The wet perovskite film was quickly put into a sample chamber connected to vacuum-pumping instrumentation (Internal space is 12 cm × 12 cm × 2.1 cm). By opening the valve connecting the specimen chamber to the pump system, the perovskite film was immediately exposed to low pressure maintained at 10 Pa for 30 s, followed by full pressurization by admitting ambient air into the specimen chamber. Subsequently, the perovskite film was annealed at 100 °C for 15 min in the air (RH = 30 ± 10%, Temperature = 25 ± 5 °C) for full crystallization. For devices prepared in N₂ environment, all operating procedures are carried out in a glove box.

1.58 eV-Cs_{0.05}(FA_{0.95}MA_{0.05})_{0.95}Pb(I_{0.95}Br_{0.05})₃: 718.335 mg PbI₂, 28.2 mg PbBr₂, 19.5 mg CsI, 8 mg MABr, 238.2 mg FAI, and 15.2 mg MACl were dissolved in 1 ml DMF and DMSO mixed solvent with a volume ratio of 4:1 to form 1.4 M stoichiometric solution. For the 1.58 eV perovskite film crystallization, the perovskite precursor solution of 100 μl was rotated for 10 s and 40 s at 2000 rpm and 5000 rpm, respectively, and 160 μl anti-solvent CB was rapidly dropped into the solution at 45 s. The precursor perovskite film was transferred to the hot plate and annealed at 100 °C for 30 min.

1.66 eV-WBG Cs_{0.05}MA_{0.15}FA_{0.8}Pb(I_{0.76}Br_{0.24})₃: 18.2 mg of CsI, 192.6 mg of FAI, 536 mg of PbI₂ (10% of excess), 131 mg of PbBr₂, and 23.5 mg MABr were dissolved in 1 ml DMF and DMSO mixed solvent with a volume ratio of 4:1 to form 1.4 M stoichiometric solution. For the 1.66 eV-Cs_{0.05}MA_{0.15}FA_{0.8}Pb(I_{0.76}Br_{0.24})₃ film crystallization, the perovskite solution of 100 μl was rotated for 5 s and 30 s at 1000 rpm and 5000 rpm, respectively, and 200 μl anti-solvent CB was rapidly dropped into the solution at 20 s. The precursor perovskite film was transferred to the hot plate and annealed at 100 °C for 15 min in the air (RH = 30 ± 10%, Temperature = 25 ± 5 °C) for full crystallization.

Device fabrication

Fabrication of small-area PSCs. First, ITO substrate was etched by laser etching technology. Ultrasonic cleaning of ITO glass after etching was carried out with glass cleaning agent, deionized water, and ethanol in sequence, and each step took 15 min. The wettability of the ITO substrate was enhanced by UV-ozone modification for 15 min. Then, the water-based ink of NiO_x nanoparticles (30 mg NiO_x nanoparticles dispersed into 1 ml deionized water) was coated on ITO glass at 4000 rpm for 30 s and annealed at 150 °C for 10 min at room temperature. After annealing, the ITO/NiO_x substrate was quickly transferred into an N₂-filled glove box for subsequent preparation. 2PACz (1 mg/ml dissolved in IPA, ultrasonic bath for 10 min) or Me-4PACz solution (0.5 mg/ml dissolved in IPA, ultrasonic bath for 10 min) was coated at 4000 rpm for 20 s on ITO/NiO_x substrate and then annealed at 150 °C for 10 min. The preparation and crystallization processes of various types of perovskites are described in the previous experimental section. For BGTS, VBETS, and LBETS-modified perovskite film, spin coating 0.5 mg/ml IPA solution of BGTS, VBETS, and LBETS on the crystallized perovskite film at 5000 rpm for 30 s, and annealing at 100 °C for 5 min. Then, for 1.58 eV-Cs_{0.05}(FA_{0.95}MA_{0.05})_{0.95}Pb(I_{0.95}Br_{0.05})₃ and WBG 1.66 eV-Cs_{0.05}MA_{0.15}FA_{0.8}Pb(I_{0.76}Br_{0.24})₃-perovskite-based solar cells, spin-coating PC₆₁BM-solution (23 mg PC₆₁BM dissolved in 1 ml CB) for 30 s at a speed of 1500 rpm. For the 1.53 eV-Cs_{0.05}MA_{0.05}FA_{0.9}PbI₃-based solar cells and modules, about 30 nm C₆₀ was thermally evaporated on the perovskite films under a high vacuum 8×10^{-4} Pa; Next, spin-coating of BCP solution (0.5 mg BCP dissolved in 1 ml IPA; filtered with a 0.22 μm PTFE filter) on PC₆₁BM layer at a speed of 5000 rpm for 30 s. Finally, the 80 nm Cu, Ag, or Au electrode is thermally evaporated at the top. For sealing the devices for MPP stability testing, a UV-curable adhesive (Eversolar AB-341, Everlight Chemical) was applied over the active area of the perovskite solar cells, followed by the placement of a highly transparent glass panel. The device was then compressed and cured under ultraviolet light for 3 min.

Fabrication of large-area PSC modules. The preparation process of 1.53 eV-Cs_{0.05}MA_{0.05}FA_{0.9}PbI₃ perovskite-based large-area modules is similar to that of small-area devices. Specifically, it is needed to evenly disperse 1 mL of Cs_{0.05}MA_{0.05}FA_{0.9}PbI₃ precursor solution on the surface of the ITO substrate, after which is needed to rest for 10 s to achieve automatic dispersion of the perovskite precursor solution on the substrate for the following spin-coating process at 2500 rpm for 20 s. The assembly of subcells in the modules involved a three-stage laser etching technique (P1, P2, P3) on a 6*10 cm² ITO substrate, creating 14 subcells. Initially, P1 targets the ITO substrates for etching, achieving a width of 30 ± 3 μm using a 1064 nm, nanosecond laser. This step involves single optical path etching, ensuring that the insulation resistance between adjacent conductive layers post-etch exceeds 10 MΩ. Importantly, the P1 process leaves no residual TCO film within the etched tracks and does not harm the underlying glass. The second etching step, P2, processes layers of ITO/NiO_x/Me-4PACz/Perovskite/C₆₀/BCP, etching to a width of 50 ± 5 μm using a 532 nm picosecond laser. The P2 laser meticulously avoids penetrating the bottom TCO layer, maintaining a precise 30 μm gap between P1 and P2 etchings. P3, the final stage, is employed for etching Au electrodes, matching the width specifications of P1 (30 ± 3 μm) using a 532 nm, picosecond laser. Similar to P2, P3 does not penetrate the bottom TCO layer, preserving a 30 μm interval between the P2 and P3 etchings.

Fabrication of tandem solar cells. The TSC device is built on a HJT silicon substrate. The wafer surface was finely polished for optimal quality. In the fabrication of a tandem device, HJT silicon substrates were initially sectioned into 12 mm × 12 mm squares using a laser. Subsequently, a perovskite sub-cell was constructed atop the HJT Si sub-cell,

employing a fabrication technique similar to that used in the creation of perovskite single-junction devices. The thicknesses of the C₆₀/BCP as electron transporting layers and the perovskite absorbers were meticulously adjusted through the spin-coating or evaporation duration. The standard active area for these tandem devices was maintained at 1.0 cm².

Device characterization. The *J-V* characteristics were obtained using a Keithley 2400 source meter in a controlled environment simulating AM 1.5 solar irradiance (100 mW cm⁻²), facilitated by a standard xenon lamp solar simulator (7ISO503A, SOFN INSTRUMENTS). For small area devices, these measurements were conducted either via a forward scan, ranging from -0.1 to 1.4 V, or a reverse scan, from 1.4 V down to -0.1 V. The *J-V* measurements for the solar cells were conducted in ambient air conditions. The external quantum efficiency (EQE) was determined using an EQE measurement system from EnliTech, Taiwan. All assessments were performed at room temperature in an ambient atmosphere, and the solar cells were not encapsulated during these measurements.

Certification of PSCs. The PSC devices were sent to the Tianjin Institute of Metrological Supervision and Testing, China, for official certification. Specifically, we fill the prepared solar cell samples for certification testing with nitrogen, then store them with a vacuum sealer and always place them in a dark sealed box. During the certification test, the certification agency recalibrates the effective active area of our solar cells to ensure accurate evaluation of data such as photocurrent density. The test environment and test methods are recorded in the certification data in Supplementary Figs. 14–20.

Characterization of device stability. The operational MPPT stability of the encapsulated devices was assessed under continuous one-sun conditions using a white LED lamp without a UV filter in a 99.99% nitrogen environment. These tests were conducted using an MPP tracking system (YH-VMPP-16, Yanghua, Suzhou). Specifically, 16 solar cell samples were simultaneously placed in aging equipment. The environment around solar cells is maintained at around 25 °C through a refrigeration system. Aging equipment is tracked and tested by continuously scanning and analyzing the maximum power point of the device. The interval between each test is 8.01 h. White LED light sources have a light intensity energy of approximately 100 mW cm⁻². The cyclic *J-V* stability of tandem devices is obtained through interval testing of their *J-V* curves. The scanning interval is 124.8 min. The recording was done using the Keithley 2400 digital source meter, and the data was obtained using the Zeal Young software K2400 Experimental Platform-Professional2450 V3.5. The long-term stability was conducted in ambient conditions at a relative humidity (RH) of 35 ± 5% and a temperature of 23 ± 5 °C.

Characterization morphology of perovskite films. Field-emission SEM (JEOL 7610 F) was used to scan the surface morphology of the film and the cross-sectional view of the device at 3 kV.

Photoluminescence and ultraviolet-visible absorption measurements. The SSPL and TRPL were measured by a fluorescence spectrometer (FLS1000, Edinburgh Instruments) with an excitation wavelength of 475 nm and an emission wavelength of ~800 nm. The ultraviolet-visible absorption spectra of the films were measured using a Shimadzu UV-1900 spectrophotometer.

Atomic force microscope measurements. The Asylum Research MFP-3D was used to measure AFM morphology and KPFM in tapping mode.

X-ray photoelectron spectroscopy and ultraviolet photoelectron spectroscopy measurements. XPS and UPS spectra were collected

through Thermo ESCALAB XI+. Fourier transform infrared (FTIR) spectroscopy was recorded using the FTIR-805 spectrometer of Tianjin Gangdong SCI.&TECH. CO.,LTD.

Laser beam-induced current LBIC measurements. LBIC was tested by LSD4 of ENLITECH, Taiwan. LBIC was used to map the local performance of photovoltaic devices by scanning a focused 405 nm light beam across the surface, generating electron-hole pairs and a measurable photocurrent. This creates a spatial map that reveals variations in photoelectric efficiency and identifies defects.

Mott-Schottky and electrochemical impedance spectroscopy measurements. The Mott-Schottky measurements were performed using the AMETEK VersSTAT 3 F electrochemical workstation at a fixed frequency of 1 kHz. The applied bias voltage range is 0 V–1.5 V. EIS measurements are made in the dark, with frequencies ranging from 0.1 Hz to 1,000,000 Hz, using the same instruments as the Mott-Schottky measuring instruments.

Transient photocurrent and photovoltage measurements. TPC/TPV was tested by PD-RS of ENLITECH, Taiwan.

Density functional theory calculation. The DFT calculations are performed using a Perdew-Burke-Ernzerhof (PBE) exchange-correlation functional. Projector augmented-wave (PAW) pseudopotentials are employed with a plane-wave cutoff energy of 400 eV. The DFT-D3 method is used for describing van der Waals interactions. The FAPbI₃ (001) surface is modelled by a slab consisting of seven atomic layers and a vacuum gap of 40 Å. The bottom two atomic layers in the slab are fixed during structural relaxation. The convergence criteria for the atomic force is set to 0.02 eV/Å. The binding energy of the ligand with the FAPbI₃ surface is defined as $E_b = E(\text{slab@ligand}) - E(\text{slab}) - E(\text{ligand})$. The electrostatic potentials (ϕ) of the passivators are calculated using the Gaussian 09 package at the B3LYP/def2TZVP level with DFT-D3.

Reporting summary

Further information on research design is available in the Nature Portfolio Reporting Summary linked to this article.

Data availability

The authors declare that the data supporting the findings of this study are available within the article and its Supplementary Information files. Additional details that support the findings of this study will be made available by the corresponding author upon request. Source data are provided with this paper.

References

- Paik, M. J. et al. Ultrafine SnO₂ colloids with enhanced interface quality for high-efficiency perovskite solar cells. *Joule* **8**, 2073–2086 (2024).
- Chen, H. et al. Improved charge extraction in inverted perovskite solar cells with dual-site-binding ligands. *Science* **384**, 189–193 (2024).
- Liu, B. et al. Interfacial defect passivation and stress release via multi-active-site ligand anchoring enables efficient and stable methylammonium-free perovskite solar cells. *ACS Energy Lett.* **6**, 2526–2538 (2021).
- Green, M. A. et al. Solar cell efficiency tables (Version 63). *Prog. Photovoltaics: Res. Appl.* **32**, 3–13 (2024).
- Li, H. et al. 2D/3D heterojunction engineering at the buried interface towards high-performance inverted methylammonium-free perovskite solar cells. *Nat. Energy* **8**, 946–955 (2023).
- Zhang, C. et al. Crystallization manipulation and holistic defect passivation toward stable and efficient inverted perovskite solar cells. *Energy Environ. Sci.* **16**, 3825–3836 (2023).
- Chen, P. et al. Multifunctional ytterbium oxide buffer for perovskite solar cells. *Nature* **625**, 516–522 (2024).
- Zhang, Z. et al. Suppressing ion migration by synergistic engineering of anion and cation toward high-performance inverted perovskite solar cells and modules. *Adv. Mater.* **36**, 2313860 (2024).
- Peng, W. et al. Reducing nonradiative recombination in perovskite solar cells with a porous insulator contact. *Science* **379**, 683–690 (2023).
- Zhang, S. et al. Minimizing buried interfacial defects for efficient inverted perovskite solar cells. *Science* **380**, 404–409 (2023).
- Yu, S. et al. Homogenized NiO_x nanoparticles for improved hole transport in inverted perovskite solar cells. *Science* **382**, 1399–1404 (2023).
- Tan, Q. et al. Inverted perovskite solar cells using dimethylacridine-based dopants. *Nature* **620**, 545–551 (2023).
- Cheng, Y. et al. Pushing commercialization of perovskite solar cells by improving their intrinsic stability. *Energy Environ. Sci.* **14**, 3233–3255 (2021).
- Li, N. et al. Towards commercialization: the operational stability of perovskite solar cells. *Chem. Soc. Rev.* **49**, 8235–8286 (2020).
- Ma, S. et al. Development of encapsulation strategies towards the commercialization of perovskite solar cells. *Energy Environ. Sci.* **15**, 13–55 (2022).
- He, D. et al. Synergistically stabilizing hole transport layer and dual interface enables high-performance perovskite solar cells. *ACS Energy Lett.* **9**, 2615–2625 (2024).
- Chen, J. et al. Causes and solutions of recombination in perovskite solar cells. *Adv. Mater.* **31**, 1803019 (2019).
- Ni, Z. et al. Resolving spatial and energetic distributions of trap states in metal halide perovskite solar cells. *Science* **367**, 1352–1358 (2020).
- Chen, J. et al. Materials and methods for interface engineering toward stable and efficient perovskite solar cells. *ACS Energy Lett.* **5**, 2742–2786 (2020).
- Park, J.-H. et al. Reduction of hole carriers by van der Waals contact for enhanced photoluminescence quantum yield in two-dimensional tin halide perovskite. *ACS Energy Lett.* **8**, 3536–3544 (2023).
- Remmerswaal, W. H. M. et al. Quantifying non-radiative recombination in passivated wide-bandgap metal halide perovskites using absolute photoluminescence spectroscopy. *Adv. Energy Mater.* **14**, 2303664 (2024).
- Yuan, Y. et al. Ion migration in organometal trihalide perovskite and its impact on photovoltaic efficiency and stability. *Acc. Chem. Res.* **49**, 286–293 (2016).
- Zhang, H. et al. Benzothieno[3,2-b]thiophene-based noncovalent conformational lock achieves perovskite solar cells with efficiency over 24%. *Angew. Chem. Int. Ed.* **135**, e202314270 (2023).
- Liu, C. et al. Bimolecularly passivated interface enables efficient and stable inverted perovskite solar cells. *Science* **382**, 810–815 (2023).
- Ye, F. et al. Overcoming C₆₀-induced interfacial recombination in inverted perovskite solar cells by electron-transporting carborane. *Nat. Commun.* **13**, 7454 (2022).
- Chen, B. et al. Imperfections and their passivation in halide perovskite solar cells. *Chem. Soc. Rev.* **48**, 3842–3867 (2019).
- Azmi, R. et al. Damp heat-stable perovskite solar cells with tailored-dimensionality 2D/3D heterojunctions. *Science* **376**, 73–77 (2022).
- Wang, T. et al. Dimensional regulation from 1D/3D to 2D/3D of perovskite interfaces for stable inverted perovskite solar cells. *J. Am. Chem. Soc.* **146**, 7555–7564 (2024).
- Azmi, R. et al. Double-side 2D/3D heterojunctions for inverted perovskite solar cells. *Nature* **628**, 93–98 (2024).
- Li, Z. et al. Organometallic-functionalized interfaces for highly efficient inverted perovskite solar cells. *Science* **376**, 416–420 (2022).

31. Yan, N. et al. Surface reconstruction for efficient NiO_x-based inverted perovskite solar cells. *Adv. Mater.* **36**, 2403682 (2024).
32. Zhuang, Q. et al. Synergistic modification of 2D perovskite with alternating cations in the interlayer space and multisite ligand toward high-performance inverted solar cells. *Adv. Mater.* **35**, 2303275 (2023).
33. Jiang, Q. et al. Surface reaction for efficient and stable inverted perovskite solar cells. *Nature* **611**, 278–283 (2022).
34. Liu, J. et al. Alkyl chains tune molecular orientations to enable dual passivation in inverted perovskite solar cells. *Angew. Chem. Int. Ed.* **63**, e202403610 (2024).
35. Zheng, Y. et al. Towards 26% efficiency in inverted perovskite solar cells via interfacial flipped band bending and suppressed deep-level traps. *Energy Environ. Sci.* **17**, 1153–1162 (2024).
36. Ma, Y. et al. Bi-molecular kinetic competition for surface passivation in high-performance perovskite solar cells. *Energy Environ. Sci.* **17**, 1570–1579 (2024).
37. Chen, J. et al. Nonhalide materials for efficient and stable perovskite solar cells. *Small Methods* **5**, 2100311 (2021).
38. Bai, L. et al. Ion migration suppression mechanism via 4-sulfobenzoic acid monopotassium salt for 22.7% stable perovskite solar cells. *Sci. China Mater.* **65**, 3368–3381 (2022).
39. Tan, S. et al. Stability-limiting heterointerfaces of perovskite photovoltaics. *Nature* **605**, 268–273 (2022).
40. Liu, B. et al. Stabilizing top interface by molecular locking strategy with polydentate chelating biomaterials toward efficient and stable perovskite solar cells in ambient air. *Adv. Mater.* **36**, 2312679 (2024).
41. Liu, B. et al. Polydentate ligand reinforced chelating to stabilize buried interface toward high-performance perovskite solar cells. *Angew. Chem. Int. Ed.* **63**, e202317185 (2024).
42. Wu, Y. et al. Thermally stable MAPbI₃ perovskite solar cells with efficiency of 19.19% and area over 1 cm² achieved by additive engineering. *Adv. Mater.* **29**, 1701073 (2017).
43. He, D. et al. Unraveling abnormal buried interface anion defect passivation mechanisms depending on cation-induced steric hindrance for efficient and stable perovskite solar cells. *J. Energy Chem.* **80**, 1–9 (2023).
44. Yang, S. et al. Regulating the electrochemical reduction kinetics by the steric hindrance effect for a robust Zn metal anode. *Energy Environ. Sci.* **17**, 1095–1106 (2024).
45. Li, X. et al. Understanding steric hindrance effect of solvent molecule in localized high-concentration electrolyte for lithium metal batteries. *Carbon Neutrality* **2**, 34 (2023).
46. Wang, L. et al. [PbX₆]⁴⁻ modulation and organic spacer construction for stable perovskite solar cells. *Energy Environ. Sci.* **15**, 4470–4510 (2022).
47. Duijnste, E. A. et al. Toward understanding space-charge limited current measurements on metal halide perovskites. *ACS Energy Lett.* **5**, 376–384 (2020).
48. Liang, J. et al. Origins and influences of metallic lead in perovskite solar cells. *Joule* **6**, 816–833 (2022).
49. Pan, Y. et al. Surface chemical polishing and passivation minimize non-radiative recombination for all-perovskite tandem solar cells. *Nat. Commun.* **15**, 7335 (2024).
50. Yao, Y. et al. The interface degradation of planar organic–inorganic perovskite solar cell traced by light beam induced current (LBIC). *RSC Adv.* **7**, 42973–42978 (2017).
51. Wang, S. et al. Tailoring the mercaptan ligands for high performance inverted perovskite solar cells with efficiency exceeding 21%. *J. Energy Chem.* **60**, 169–177 (2021).
52. Zhu, Y. et al. Heterointerface energetics regulation strategy enabled efficient perovskite solar cells. *Adv. Energy Mater.* **14**, 2303946 (2024).
53. Zhao, X. et al. Rationally tailoring chiral molecules to minimize interfacial energy loss enables efficient and stable perovskite solar cells using vacuum flash technology. *Nano Lett.* **23**, 11184–11192 (2023).
54. Fang, Z. et al. CsPbI_{2.25}Br_{0.75} solar cells with 15.9% efficiency. *Sci. Bull.* **64**, 507–510 (2019).

Acknowledgements

This work was supported by the Science and Technology Development Fund, Macau SAR (No. 0009/2022/AGJ, J.T.). The National Natural Science Foundation of China (U21A2076 (C.C.), 62274018 (J.C.), 52462031 (C.C.), 22279149 (Y.W.)). The S&T Program of Hebei (24464401D, C.C.). The Central Guidance on Local Science and Technology Development Fund of Hebei Province (226Z4305G, C.C.). Hebei Province Higher Education Science and Technology Research Project (JZX2024030, C.C.). Shijiazhuang Basic Research Project at Hebei-based Universities (241790847 A, C.C.). Youth Innovation Promotion Association of the Chinese Academy of Sciences (No. 2022034, Y.W.). The Natural Science Foundation of Hebei Province (E2024202086 (C.C.), E2024202300 (C.C.)). H.Z. acknowledges the funding support from the National Natural Science Foundation of China (No. 52302229).

Author contributions

Z.Z., Y.F., J.C., J.T., and C.C. conceived the ideas of the work and carried out the basic characterization, including *J-V* and EQE photovoltaic measurement. Y.F., J.D., Q.M. and Z.Z. prepared the small active area perovskite samples and PSC devices, and performed most measurements, including KPFM, AFM, SCLC, LBIC and MPP stability. M.L., T.G., and W.G. assisted with FTIR and XPS measurements. W.G. and Y.F. performed SEM measurements. B. Z. helped to conduct the TRPL and PL measurements and analysis. Y.F., Y.W. Q.M., and C.C. conducted the fabrication of tandem solar cells. Y.F. and J.D. certified the efficiency of the PSCs. Z.Z., H.C. and C.C. conducted the long-term cyclic *J-V* stability measurements. Y.F. and Y.W. completed the preparation and testing of large-area PSC module devices. Y.F., C.C. and J.C. wrote the first draft of the manuscript. H. Z. and T. P. were involved in the data analysis. C.C. and J.C. wrote the final version of the manuscript. J.T., J.C. and C.C. supervised this project. All authors analyzed the data and contributed to the discussions. Y.F., C.C., and J.Z. conducted theoretical calculation analysis.

Competing interests

The authors declare no competing interests.

Additional information

Supplementary information The online version contains supplementary material available at <https://doi.org/10.1038/s41467-025-56068-6>.

Correspondence and requests for materials should be addressed to Hong Zhang, Jiajia Zhang, Yang Wang, Jian-Xin Tang, Jiangzhao Chen or Cong Chen.

Peer review information *Nature Communications* thanks the anonymous, reviewer(s) for their contribution to the peer review of this work. A peer review file is available.

Reprints and permissions information is available at <http://www.nature.com/reprints>

Publisher's note Springer Nature remains neutral with regard to jurisdictional claims in published maps and institutional affiliations.

Open Access This article is licensed under a Creative Commons Attribution-NonCommercial-NoDerivatives 4.0 International License, which permits any non-commercial use, sharing, distribution and reproduction in any medium or format, as long as you give appropriate credit to the original author(s) and the source, provide a link to the Creative Commons licence, and indicate if you modified the licensed material. You do not have permission under this licence to share adapted material derived from this article or parts of it. The images or other third party material in this article are included in the article's Creative Commons licence, unless indicated otherwise in a credit line to the material. If material is not included in the article's Creative Commons licence and your intended use is not permitted by statutory regulation or exceeds the permitted use, you will need to obtain permission directly from the copyright holder. To view a copy of this licence, visit <http://creativecommons.org/licenses/by-nc-nd/4.0/>.

© The Author(s) 2025